Geomechanics and Engineering, *Vol. 29, No. 2 (2022) 113-131*
https://doi.org/10.12989/gae.2022.29.2.113

Modeling of a rockburst related to anomalously low friction effects in great depth

J.W. Zhan[1a], G.X. Jin*[2], C.S. Xu[4b], H.Q. Yang[5c], J.F. Liu[5d] and X.D. Zhang[3e]

[1]*College of Civil Engineering, Fujian University of Technology, Fuzhou, China*
[2]*College of Ecological Environment and Urban Construction, Fujian University of Technology, Fuzhou, China*
[3]*College of Civil Engineering, Fuzhou University, Fuzhou, China*
[4]*School of Civil, Environment and Mining Engineering, the University of Adelaide, Adelaide*
[5]*School of Civil Engineering, Chongqing University, Chongqing, China*

(Received October 25, 2018, Revised December 18, 2021, Accepted February 21, 2022)

Abstract. A rockburst is a common disaster in deep-tunnel excavation engineering, especially for high-geostress areas. An anomalously low friction effect is one of the most important inducements of rockbursts. To elucidate the correlation between an anomalously low friction effect and a rockburst, we establish a two-dimensional prediction model that considers the discontinuous structure of a rock mass. The degree of freedom of the rotation angle is introduced, thus the motion equations of the blocks under the influence of a transient disturbing force are acquired according to the interactions of the blocks. Based on the two-dimensional discontinuous block model of deep rock mass, a rockburst prediction model is established, and the initiation process of ultra-low friction rockburst is analyzed. In addition, the intensity of a rockburst, including the location, depth, area, and velocity of ejection fragments, can be determined quantitatively using the proposed prediction model. Then, through a specific example, the effects of geomechanical parameters such as the different principal stress ratios, the material properties, a dip of principal stress on the occurrence form and range of rockburst are analyzed. The results indicate that under dynamic disturbance, stress variation on the structural surface in a deep rock mass may directly give rise to a rockburst. The formation of rockburst is characterized by three stages: the appearance of cracks that result from the tension or compression failure of the deformation block, the transformation of strain energy of rock blocks to kinetic energy, and the ejection of some of the free blocks from the surrounding rock mass. Finally, the two-dimensional rockburst prediction model is applied to the construction drainage tunnel project of Jinping II hydropower station. Through the comparison with the field measured rockburst data and UDEC simulation results, it shows that the model in this paper is in good agreement with the actual working conditions, which verifies the accuracy of the model in this paper.

Keywords: anomalously low friction; intensity; prediction model; rockburst; tunnel

1. Introduction

A rockburst is defined as a violent explosion of a block causing a sudden rupture in the rock. Rockbursts are quite common in deep tunnels (Li *et al.* 2019). A rockburst can be accompanied by rock splitting, flake peeling, ejection of rock pieces with noise, and even the sudden collapse of a tunnel (He *et al.* 2018, Keneti and Sainsbury 2018, Ma *et al.* 2018). Due to their frequent occurrence and terrible destruction, rockbursts in deep rock masses have drawn the attention of many engineers and scientists. When a rockburst phenomenon occurs, the existing support design and tunneling methods must be reconsidered carefully (Ulusay 2016).

To investigate the prediction of rockbursts, methods based on the strength criterion have been introduced, such as the Russense (1974), Barton *et al.* (1974), Turchaninov (Turchaninov, 1981), and Hoek methods (Hoek and Brown 1980), Huang *et al.* (2017), Wang *et al.* (2018). These methods mainly depend on the ratio between the uniaxial compressive strength and parameters such as the tangential stress, maximum geostress, and axial stress of caverns. Many laboratory tests were conducted to obtain these data. Considering the transformation of energy during a rockburst, scholars have proposed various energy theories, including the energy consumption index method (Kidybinski 1981), orientation index method (Mazaira and Konicek 2015), and energy ratio method (Chen *et al.* 2015). Pu *et al.* (2019) employed a support vector classifier (SVC) to predict rockburst in kimberlite pipes at a diamond mine, and the processed prediction data was fed into the trained SVC model, the prediction results were obtained, which matched

*Corresponding author, Professor, Lecturer
E-mail: jinguixiao2008@126.com
[a]Lecturer
E-mail: zhanjinwu1989@foxmail.com
[b]Ph.D.
E-mail: chaoshui.xu@adelaide.edu.au
[c]Ph.D.
E-mail: 1229278575@qq.com
[d]Ph.D.
E-mail: 1306661897@qq.com
[e]Ph.D.
E-mail: 258621476@qq.com

ISSN: 2005-307X (Print), 2092-6219 (Online)

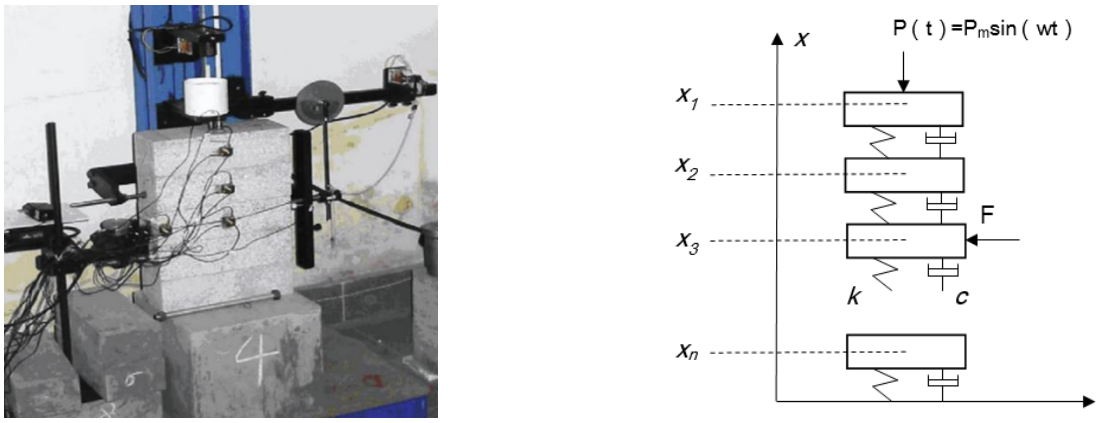

(a) Experimental model (b) Theoretical model

Fig. 1 Anomalous low friction effect model: (a) experimental model and (b) theoretical model (Wu *et al*. 2008)

real rockburst cases that recently occurred at this mine. Zou (2016) proposed an approximate solution of a circular tunnel based on the generalized Hoek-Brown failure criterion. Many other methods, mainly based on experimental approaches, have been proposed, such as a brittleness index method (Shi *et al.* 2021) and a supervised learning method (Zhou and Mitri 2016).

The above methods are mainly based on laboratory tests and mechanical theory. Although the relations between the influencing factors and rockbursts were studied, those methods are insufficient in both explaining the inner rockburst mechanism and simulating the real state of the deep rock mass. To overcome this deficiency, field test methods were adopted, through which real-time data could be acquired (Stacey 2016). Also, the corresponding relationship between the monitoring information and the specific phenomenon occurring in excavation could be established. So far, techniques such as acoustic emission (Hardy 1972, Lei *et al.* 2000), the microgravity method (Fajklewicz 1983), and the electromagnetic radiation method (Frid 2001) have been used to establish the corresponding relationship between them. In particular, Yang *et al.* (2019) adopted the borehole overcoring method to carry out the in-situ stress for field test, and judged the rock burst level of the tunnel according to the russens criterion. But the shortcomings of in situ tests are obvious, such as the high expense and poor anti-interference performance.

On the other hand, to use only one method to predict the probability of rockbursts has limited accuracy and reliability. Therefore, it is necessary to establish an appropriate evaluation method to assess the tendency of rockburst accurately by considering multiple influencing factors. Many mathematical evaluation methods have been adopted for this purpose. Familiar methods are fuzzy mathematics (Wang *et al.* 2015, Wang *et al.* 2019), neural networks (Di and Wang, 2021), ant colony optimization (Dorigo and Birattari 2010), and improved support vector machines (Ji *et al.* 2020).

Numerical methods have also been widely used to predict rockbursts. Based on the boundary element method, Shen (2011) modeled the fracturing process in a surrounding rock mass using the FRACOD program. Zuo (2012) performed numerical analysis on the zonal disintegration of rock mass using realistic failure process analysis (RFPA3D). Shi and Chen (2014) conducted numerical simulation research on a deeply buried coal roadway fault rockburst. He *et al.* (2016) proposed a discontinuous rock-mass model to predict rockbursts.Based on finite element model (FEM) software, the Abaqus explicit code was used to simulate dynamic rock failure in deep tunnels. Material heterogeneity was considered using Python scripting in Abaqus, and Rockbursts near fault regions in deep tunnels under static and dynamic loads were studied (Manouchehrian and Cai 2017). Sepehri *et al.* (2020) used the results of the numerical model, two rockburst criteria (Ts and BPI) have been used to assess the rockburst tendency in the understudy domain.

Most current predictive methods can only evaluate the probability of occurrence of rockbursts. However, it can not predict the location, range and strength of rockburst from present models. Since the quantitative level is not sufficiently applicable as a basis for further research in rockburst prevention, it is necessary to develop a new rockburst prediction method. Sadovsky (1979) proposed that it is necessary to account for the discrete structure of a real rock mass. The discrete structures of the material at various scale levels were considered in the solution of the dynamic crack propagation problem (Slepyan 2012, Kazarinov *et al.* 2021). Aleksandrova (2004) used the visco-elastic and elastic models to simulate wave propagation in block media. Kurlenya (1998) first discovered a phenomenon that occurs among deep masses: the friction among interacting geo-blocks disappears quasi-periodically at some discrete points along the direction orthogonal to the external pulse. For this reason, the phenomenon was later named anomalous low friction (ALF). As one of the typical nonlinear dynamic responses in deep rock masses, the ALF phenomenon is related to rockburst, especially the fault movement of rockburst in deep coal mine excavation (Wu *et al.* 2008). And more experimental investigations of the ALF phenomenon were conducted by Wu *et al*. (2008), who explored and explained the ALF phenomenon by establishing a similar one-dimensional dynamic analysis

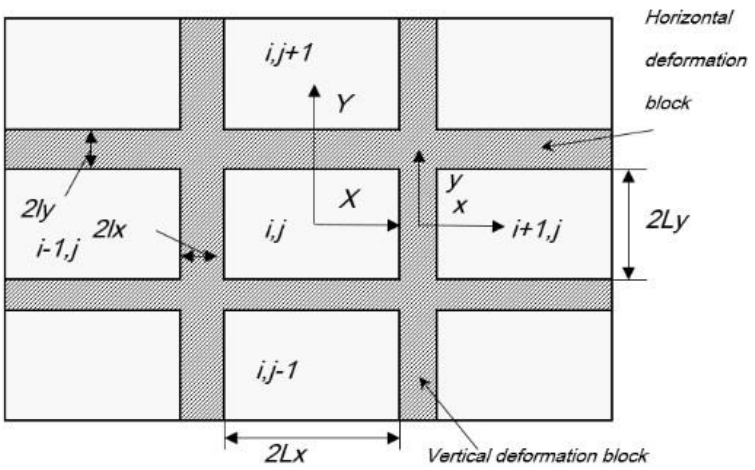

Fig. 2 Two-dimensional discontinuous block model, in which the shaded areas stand for deformation blocks and the other spaces represent rigid blocks

experimental model in different materials. The corresponding numerical model was also built (see Fig. 1).

The research on the occurrence mechanism, prediction mechanism and preventive measures of rock burst is also promoted by scholars all over the world. However, there are many reports of disasters and accidents caused by rock burst to deep engineering, and the problem of high death rate of rock burst has not been well solved. Therefore, the research on rockburst prediction still needs to be carried out.

The purpose of this paper is to clarify the physical mechanism of rockburst generation due to the ALF phenomenon in an elastic rock mass. On this basis, a more quantitative rockburst prediction model is established compared with the previous prediction. By extending from Saraikin's model (Saraikin *et al*. 1998), the proposed model can evaluate the detailed intensity parameters of rockburst such as the location, depth, rockburst area, and velocity of ejected pieces. Specifically, to explain the mechanism of an anomalous low-friction type rockburst, the formation of the rockburst is illustrated, step by step. The changing behavior of the rockburst configuration in the tunnel's radial direction is comprehensively studied. The results can provide guidance on the design and construction of deep excavated tunnels.

2. Two-dimensional discontinuous block model

2.1 Construction of the two-dimensional discontinuous block model

In this section, a two-dimensional discontinuous block model is established on the basis of the one-dimensional discontinuous block model. The degree of freedom of the rotation angle is introduced, thus the motion equations of the blocks under the influence of the transient disturbing force are acquired according to the interactions of the blocks.

As shown in Fig. 2, the two-dimensional discontinuous block model consists of rigid blocks and deformation blocks.

The length of rigid blocks in the x- and y-directions are $2L_x$ and $2L_y$, respectively. The deformation blocks are divided into two kinds: vertical deformation blocks with a length of $2l_x$ in the x-direction and $2L_y$ in the y-direction, and horizontal deformation blocks with a length of $2L_x$ in the x-direction and $2l_y$ in the y-direction. The dimensions of the deformation blocks are much less than those of the rigid blocks. This assumption corresponds to the concept of lithospheric structure defined by Sadovsky (1979), in which a hierarchy of blocks (elements) is separated by relatively thin, pliable boundary zones.

2.2 Derivation of the motion equations of the deformation blocks

For convenience in calculations, the rigid blocks are numbered using the indices i horizontally and j vertically. It is assumed that each rigid block (i, j) only interacts with its four nearest neighbor blocks: $(i, j+1)$, $(i, j-1)$, $(i+1, j)$, $(i-1, j)$. Using global coordinates, the motion of rigid block (i, j) is described by the two displacements $u_{i,j}$, $v_{i,j}$ and the rotation angle $\varphi_{i,j}$. The motion of a deformation block is described by the two displacements u_l, v_l.

Associated with its center of gravity, the motion of each rigid block in the rectangular coordinate system is described by two displacements $\overline{u}$, $\overline{v}$ and the rotation angle φ, where φ is relatively small ($|\varphi| << 1$). Then we have

$$\begin{cases} u = \overline{u} - y\varphi \\ v = \overline{v} + x\varphi \end{cases} \tag{1}$$

where u, v are the respective displacements of the block in the x- and y-directions in the coordinate system.

Assuming that the displacements of the deformation block vary linearly with the length along the x and y axial directions, then we have

for the vertical deformation block,

$$\begin{cases} u_l = a_1 + a_2 x \\ v_l = b_1 + b_2 x \end{cases} \quad (|x| \le l_x) \tag{2}$$

for the horizontal deformation block,

$$\begin{cases} u_l = a_3 + a_4 x \\ v_l = b_3 + b_4 x \end{cases} \quad (|y| \le l_y) \tag{3}$$

The coefficients a_1, …, a_4 and b_1, …, b_4 can be determined by the boundary conditions of the elastic block and the corresponding adjacent rigid blocks. Taking the left vertical deformation block and the upper horizontal deformation block (i, j) for example, we have

$$\begin{cases} u_l\big|_{x=-l_x} = u_{i,j}\big|_{X=L_x} \; u_l\big|_{x=-l_x} = u_{i+1,j}\big|_{X=-L_x} \\ v_l\big|_{x=-l_x} = v_{i,j}\big|_{X=L_x} \; v_l\big|_{x=-l_x} = v_{i+1,j}\big|_{X=-L_x} \end{cases} \tag{4}$$

$$x = \pm l_x (X = \pm L_x)$$

$$\begin{cases} u_l\big|_{y=-l_y} = u_{i,j}\big|_{Y=L_y} \; u_l\big|_{y=-l_y} = u_{i+1,j}\big|_{Y=-L_y} \\ v_l\big|_{y=-l_y} = v_{i,j}\big|_{Y=L_y} \; v_l\big|_{y=-l_y} = v_{i+1,j}\big|_{Y=-L_y} \end{cases} \tag{5}$$

$$y = \pm l_y \left(Y = \pm L_y\right)$$

Substituting Eqs. (2) and (3) into Eqs. (4) and (5), the displacements of the deformation blocks can be expressed in terms of the displacements of the rigid blocks.

For vertical deformation block (i, i+l), we have

$$\begin{cases} u_l = \frac{1}{2}\left[(u_{i+1,j} + u_{i,j} - y(\varphi_{i+1,j} + \varphi_{i,j})) + (u_{i+1,j} - u_{i,j} - y(\varphi_{i+1,j} - \varphi_{i,j}) \frac{x}{l_x} \right] \\ v_l = \frac{1}{2}\left[(v_{i+1,j} + v_{i,j} - L_x(\varphi_{i+1,j} + \varphi_{i,j})) + (v_{i+1,j} - v_{i,j} - L_x(\varphi_{i+1,j} - \varphi_{i,j})) \frac{x}{l_x} \right] \end{cases} \tag{6}$$

Similarly, for horizontal deformation block (j, j+l), we have

$$\begin{cases} u_l = \frac{1}{2}\left[(u_{i,j+1} + u_{i,j} + L_y(\varphi_{i,j+1} - \varphi_{i,j})) + (u_{i,j+1} - u_{i,j} + L_y(\varphi_{i,j+1} + \varphi_{i,j})) \frac{y}{l_y} \right] \\ v_l = \frac{1}{2}\left[(v_{i,j+1} + v_{i,j} + x(\varphi_{i,j+1} + \varphi_{i,j})) + (v_{i+1,j} - v_{i,j} + x(\varphi_{i,j+1} - \varphi_{i,j})) \frac{y}{l_y} \right] \end{cases} \tag{7}$$

Considering the elastic-brittle property of rock, the stress and displacement of the deformation block are related with Hooke's law of an elastic period. Under the two-dimensional condition, we have

$$\begin{cases} \sigma_{n_x} = (\lambda + 2\mu)\frac{\partial u_l}{\partial x} + \lambda \frac{\partial v_l}{\partial y} \\ \sigma_{n_y} = \lambda \frac{\partial u_l}{\partial x} + (\lambda + 2\mu)\frac{\partial v_l}{\partial y} \\ \tau_{xy} = \mu\left(\frac{\partial u_l}{\partial y} + \frac{\partial v_l}{\partial x}\right) \end{cases} \tag{8}$$

$$\lambda = \frac{Ev}{(1+v)(1-2v)} \tag{9}$$

$$\mu = \frac{E}{2(1+v)} \tag{10}$$

Substituting Eqs. (6) and (7) into Eq. (8), the stress in the deformation blocks can be expressed in terms of the displacements and rotation of the rigid blocks under the assumption (l_x, l_y)<<(L_x, L_y).

For a vertical deformation block

$$\begin{cases} \sigma_{n_x} = \frac{\lambda + 2\mu}{2l_x}(u_{i+1,j} - u_{i,j} - y(\varphi_{i+1,j} - \varphi_{i,j})) \\ \sigma_{n_y} = \frac{\lambda}{2l_x}(u_{i+1,j} - u_{i,j} - y(\varphi_{i+1,j} - \varphi_{i,j})) \\ \tau_{xy} = \frac{\mu}{2l_x}(v_{i+1,j} - v_{i,j} - L_x(\varphi_{i+1,j} + \varphi_{i,j})) \end{cases} \tag{11}$$

$$\begin{cases} \sigma_{n_x} = \frac{\lambda}{2l_y}(v_{i+1,j} - v_{i,j} + x(\varphi_{i,j+1} - \varphi_{i,j})) \\ \sigma_{n_y} = \frac{\lambda + 2\mu}{2l_y}(v_{i,j+1} - v_{i,j} + x(\varphi_{i,j+1} - \varphi_{i,j})) \\ \tau_{xy} = \frac{\mu}{2l_y}(u_{i,j+1} - u_{i,j} + L_y(\varphi_{i,j+1} + \varphi_{i,j})) \end{cases} \tag{12}$$

Hence, the motion equations of a rigid block (i, j) are derived. If a block is not a boundary block, we have

$$\begin{cases} m\frac{\partial^2 u_{i,j}}{\partial t^2} = \int_L p_x dl + F_x \\ m\frac{\partial^2 v_{i,j}}{\partial t^2} = \int_L p_y dl + F_y \\ J\frac{\partial^2 \varphi_{i,j}}{\partial t^2} \int_L (xp_y - yp_x) dl + M_0 \end{cases} \tag{13a}$$

where

$$m = 4\rho L_x L_y \tag{13b}$$

$$J = \frac{4}{3}\rho L_x L_y (L_x^2 + L_y^2) \tag{13c}$$

$$\begin{cases} p_x = \sigma_{n_x} n_x + \tau_{xy} n_y \\ p_y = \tau_{xy} n_x + \sigma_{n_y} n_y \end{cases} \tag{13d}$$

m and J are the mass and central moment of the block, respectively; ρ is the density of the block; p_x and p_y are the projections of the stress vector acting on a block contour L onto the respective x- and y-axes; and n_x, n_y are the projections of the normal vector to contour L onto the respective x and y axes. F_x, F_y, and M_0 are the external forces and moment applied to the block.

Substituting p_x and p_y in Eqs. (11) and (12), then

integrating the expressions on the right side of Eq. (13), the motion equations of the rigid blocks are obtained as follows

$$\frac{\partial^2 u_{i,j}}{\partial t^2}=\frac{V_1}{L_x l_x}(u_{i+1,j}-2u_{i,j}+u_{i-1,j})+\frac{V_2}{L_y l_y}(u_{i,j+1}-2u_{i,j}+u_{i,j-1}+L_y(\varphi_{i,j+1}-\varphi_{i,j-1}))+\frac{F_x}{m} \quad (14)$$

$$\frac{\partial^2 v_{i,j}}{\partial t^2}=\frac{V_2}{L_x l_x}(v_{i+1,j}-2v_{i,j}+v_{i-1,j}-L_x(\varphi_{i+1,j}-\varphi_{i-1,j}))+\frac{V_1}{L_y l_y}(v_{i,j+1}-2v_{i,j}+v_{i,j-1})+\frac{F_y}{m} \quad (15)$$

$$\begin{aligned}\frac{\partial^2 \varphi_{i,j}}{\partial t^2}&=\frac{V_1 L_y^2}{L_x l_x H^2}(\varphi_{i+1,j}-2\varphi_{i,j}+\varphi_{i-1,j})+\frac{V_1 L_x^2}{L_y l_y H^2}(\varphi_{i,j+1}-2\varphi_{i,j}+\varphi_{i,j-1})\\&-\frac{3V_2}{l_y H^2}((u_{i,j+1}-u_{i,j-1})+L_y(\varphi_{i,j+1}-2\varphi_{i,j}+\varphi_{i,j-1}))\\&+\frac{3V_2}{l_y H^2}((v_{i+1,j}-v_{i-1,j})-L_x(\varphi_{i+1,j}+2\varphi_{i,j}+\varphi_{i-1,j}))+\frac{M_0}{J}\end{aligned} \quad (16)$$

where $V_1=\dfrac{(\lambda+2\mu)}{4\rho}$, $V_2=\dfrac{\mu}{4\rho}$, $H^2=L_x{}^2+L_y{}^2$.

As for boundary blocks, the equations describing the motion of the rigid blocks must be specifically derived. The contour L in Eq. (13) must be divided into two parts; one interacts with its neighbors through the inner deformation block and the other bears external forces and moments.

We transform Eqs. (14), (15), and (16) into the finite difference expression as

$$\begin{aligned}u_{i,j}^{t+1}=&\left(\frac{V_1}{L_x l_x}\left(u_{i+1,j}^t-2u_{i,j}^t+u_{i-1,j}^t\right)+\frac{V_2}{L_y l_y}\left(u_{i,j+1}^t-2u_{i,j}^t+\right.\right.\\&\left.\left.L_y\left(\varphi_{i,j+1}^t-\varphi_{i,j-1}^t\right)\right)+\frac{F_y}{m}\right)\Delta t^2+2u_{i.j}^t-u_{i.j}^{t-1}\end{aligned} \quad (17)$$

$$\begin{aligned}v_{i,j}^{t+1}=&\left(\frac{V_2}{L_x l_x}\left(v_{i+1,j}^t-2v_{i,j}^t+v_{i-1,j}^t-L_x\left(\varphi_{i+1,j}^t-\varphi_{i-1,j}^t\right)\right)+\right.\\&\left.\frac{V_1}{L_y l_y}\left(v_{i,j+1}^t-2v_{i,j}^t+v_{i,j-1}^t\right)+\frac{F_y}{m}\right)\Delta t^2+2u_{i.j}^t-u_{i.j}^{t-1}\end{aligned} \quad (18)$$

$$\begin{aligned}\varphi_{i,j}^{t+1}=&\left(\frac{V_1 L_y^2}{L_x l_x H^2}\left(\varphi_{i+1,j}^t-2\varphi_{i.j}^t+\varphi_{i-1.j}^t\right)+\frac{V_1 L_x^2}{L_y l_y H^2}\left(\varphi_{i,j+1}^t-2\varphi_{i.j}^t+\varphi_{i.j-1}^t\right)-\right.\\&\frac{3V_2}{l_y H^2}\left(\left(u_{i,j+1}^t-u_{i,j-1}^t\right)+L_y\left(\varphi_{i,j+1}^t+2\varphi_{i.j}^t+\varphi_{i.j-1}^t\right)\right)+\frac{3V_2}{l_y H^2}\left(\left(v_{i+1,j}^t-v_{i-1,j}^t\right)-\\&\left.L_x\left(\varphi_{i+1,j}^t+2\varphi_{i.j}^t+\varphi_{i-1.j}^t\right)\right)+\frac{M_0}{J}\Delta t^2+2\varphi_{i.j}^t-\varphi_{i.j}^{t-1}\end{aligned} \quad (19)$$

An absorbing boundary is introduced to reduce boundary reflection of the finite-width numerical model. The expressions describing the blocks in the absorbing boundary are as follows.

For the right absorbing boundary

$$\begin{cases}u_{i,j}^{t+1}=u_{i,j}^t-c_1\dfrac{\Delta t}{\Delta x}\left(u_{i,j}^t-u_{i-1,j}^t\right)\\ v_{i,j}^{t+1}=v_{i,j}^t-c_2\dfrac{\Delta t}{\Delta x}\left(v_{i,j+1}^t-v_{i-1,j}^t\right)\end{cases} \quad (20)$$

for the left absorbing boundary

$$\begin{cases}u_{i,j}^{t+1}=u_{i,j}^t+c_1\dfrac{\Delta t}{\Delta x}\left(u_{i+1,j}^t-u_{i,j}^t\right)\\ v_{i,j}^{t+1}=v_{i,j}^t+c_2\dfrac{\Delta t}{\Delta x}\left(v_{i+1,j}^t-v_{i,j}^t\right)\end{cases} \quad (21)$$

for the upper absorbing boundary

$$\begin{cases}u_{i,j}^{t+1}=u_{i,j}^t+c_2\dfrac{\Delta t}{\Delta y}\left(u_{i,j}^t-u_{i,j-1}^t\right)\\ v_{i,j}^{t+1}=v_{i,j}^t+c_1\dfrac{\Delta t}{\Delta y}\left(v_{i,j}^t-v_{i,j-1}^t\right)\end{cases} \quad (22)$$

and for the lower absorbing boundary

$$\begin{cases}u_{i,j}^{t+1}=u_{i,j}^t-c_1\dfrac{\Delta t}{\Delta y}\left(u_{i,j+1}^t-u_{i,j}^t\right)\\ v_{i,j}^{t+1}=v_{i,j}^t-c_2\dfrac{\Delta t}{\Delta y}\left(v_{i,j+1}^t-v_{i,j}^t\right)\end{cases} \quad (23)$$

where c_1, c_2 are the wave velocities.

3. Quantitative prediction model of low friction-type rockburst

3.1 Theoretical analysis of the occurrence of low friction-type rockburst

Rockburst usually occurs in elasto-brittle rock. Unlike other forms of rock, the stress-strain relationship of elastic brittle rock mass has the following characteristics, when the rock mass reaches the stress peak, the strain level remains unchanged, the stress drops obviously, or even falls to zero. Then strain acutely increases while stress remains unchanged (see Fig. 3).

Consistent with this characteristic, it is assumed that the deformation blocks will turn to a failure state when the axial strain reaches its ultimate value. The failure impairs the interaction between the adjacent blocks and leads to the formation of cracks at the macro level. When the deformation sub block reaches the ultimate compressive strain or tensile strain at a certain time, the deformation sub block will be crushed or pulled, and obvious cracks will appear between the blocks. When these transverse and vertical cracks penetrate, the accumulated potential energy is converted into kinetic energy. As a result, the blocks near the free surface will more easily slip at a certain velocity. For example, in Fig. 4, When the left and right sides and upper deformation sub blocks of block A near the free face are subject to tensile failure or compression failure under excavation disturbance. Then, driven by high speed, the block A may break away from the surrounding rock and eject into the free face to form rock burst, falling into the tunnel. In the actual rock burst, this phenomenon is not limited to a block, and the peripheral deformation sub blocks of blocks with different numbers and positions may reach the failure state. In this way, rockburst phenomena with different positions, fragment sizes and fragment ejection speeds may occur.

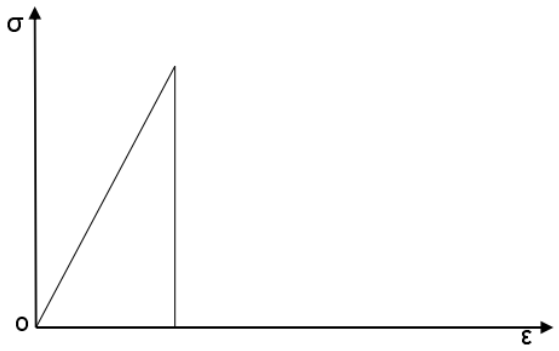

Fig. 3 The stress-strain relation of elasto-brittle rock

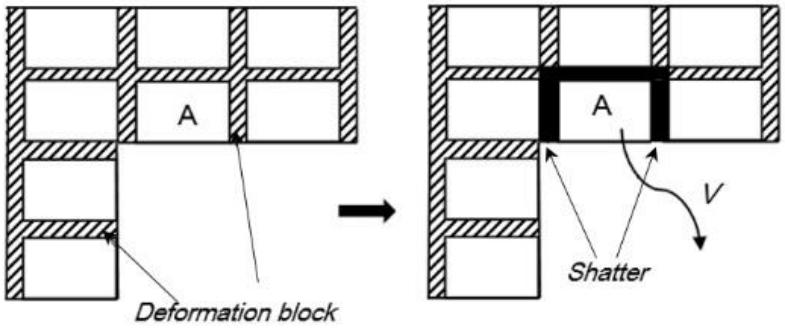

Fig. 4 Mechanism of rockburst, where block A might be driven out due to the tensile or compressive failure of the surrounding deformation blocks

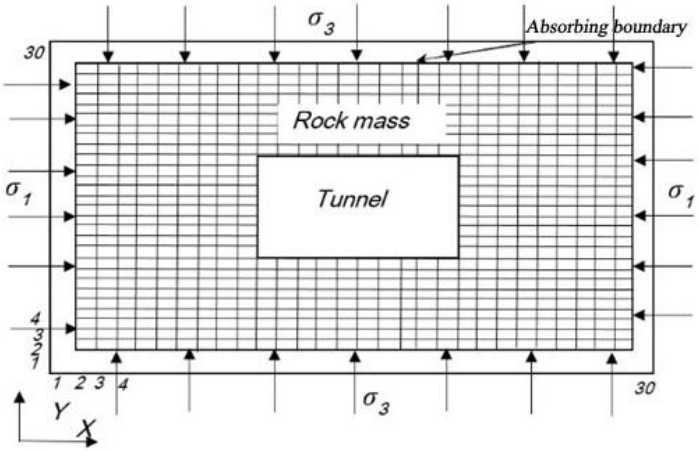

Fig. 5 Two-dimensional model of rectangle tunnel, where the large central rectangle represents the tunnel and the surrounding small rectangles represent rigid blocks

3.2 Occurrence mechanism of low friction-type roc kburst

A two-dimensional model of a rectangular tunnel is shown in Fig. 5. The model consists of 30 x 30 rigid blocks, including the absorbing boundary blocks. The excavation tunnel is equivalent to 10 x 10 blocks in the middle of the model. The horizontal and vertical geostress, denoted respectively as σ_1 and σ_3, is distributed homogeneously on the boundary.

The values of model parameters are based on a certain drainage tunnel in the second-cascade hydropower station in Jinping, and the specific parameters are as follows. The block dimensions are Lx = 1 m, Ly = 1 m, lx = 0.05 m, and ly = 0.05 m. The time step is Δt = 0.0001 s. The minimum principal stress is σ_3= 20 MPa. The maximum principal stress is σ_1 = 80 MPa. The density of a block is ρ = 2,500 kg/m^3. The Lamé constants of the deformation block are λ = 8 GPa and μ = 4 GPa. During the period 0-10,000Δt, the model is in the period of static equilibrium when the tunnel has not been excavated. During the period 10,000Δt < t < 15,000Δt, the model is under the state of excavation unloading.

According to a series of measured values obtained from indoor tensile tests (Yu *et al*. 2010), the ultimate axial tensile strain of the deformed sub block in this model is

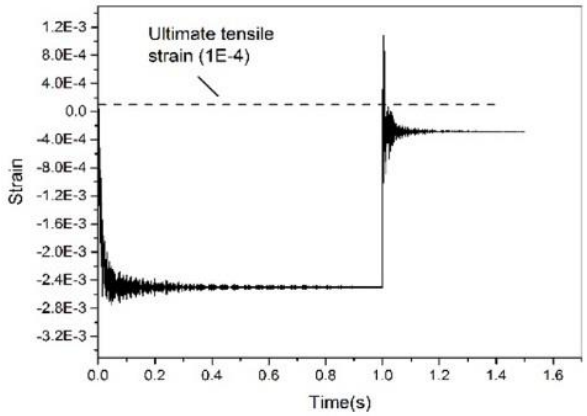

Fig. 6 Strain of the horizontal deformation block between block (15, 9) and block (15, 10) versus time

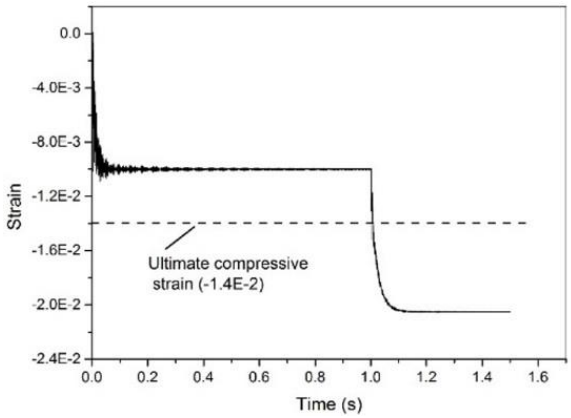

Fig. 7 Strain of the vertical deformation block between block (15, 9) and block (16, 9) versus time

1.0×10^{-4}. According to the stress-strain curve obtained from the rock axial compression experiment (Yu *et al*. 2010), the ultimate axial compressive strain of the deformation sub block is -1.4×10^{-2}. Negative represents compression and positive represents tension.

Through MATLAB programming, a two-dimensional tunnel rockburst prediction model is established, and the example above is calculated. By observing the failure phenomenon of the surrounding rock mass, the mechanism and characteristics of an anomalously low friction-type rockburst can be explained in terms of the strain-time curve of the deformation block. The analysis of the crack propagation pattern among the surrounding rock and the velocity-time curves of the blocks are presented in the following sections.

3.2.1 Analysis of the strain-time curve of the deformation blocks

Figs. 6 and 7 depict the strain-time curves of the horizontal deformation block between blocks (15, 9) and (15, 10), and the vertical deformation block between blocks (15, 9) and (16, 9). In the period of static equilibrium (0-1 s), the horizontal and vertical deformation blocks are in a compression state with strain values of -2.8×10^{-3} and -1.1×10^{-2}. The value is lower than the ultimate compressive strain-1.4×10^{-2}. Therefore, under the action of original in-situ stress, the two deformation sub blocks are in the elastic undamaged stage. After the excavation, the strain changes of the two deformation sub blocks show different trends under the disturbance of unloading. Unloading produces instantaneous tension, which makes the horizontal deformation sub block transition from compression to tension in a very short time, and finally return to compression, but the value of compressive strain decreases significantly. In this transient process, if the tensile strain reaches the limit tensile strain, the deformation sub block will be pulled out and form cracks. In Fig. 6, the strain value of the horizontal deformation sub block reaches the maximum value of 1.088×10^{-3} at 1.0035s, exceeding the set limit tensile strain value 1×10^{-4}. The horizontal deformation sub block is in a broken state and forms cracks. In the unloading process, the vertical deformation sub block is still in the compression state, and the strain value increases in the negative direction. In this instantaneous process, if the compressive strain reaches the limit compressive strain, the deformation sub block will be crushed and form cracks. In Fig. 7, the strain value of the vertical deformation sub block reaches -2.06×10^{-2} at 1.2140s, exceeding the set limit compressive strain value of -1.4×10^{-2}. According to the failure criteria set in the previous section, the vertical deformation sub block is in the crushing state and forms cracks.

3.2.2 The crack evolution pattern of the low friction-type rockburst

The crack propagation pattern of the surrounding rock is shown in Fig. 8. The dotted line in Fig. 8 shows the

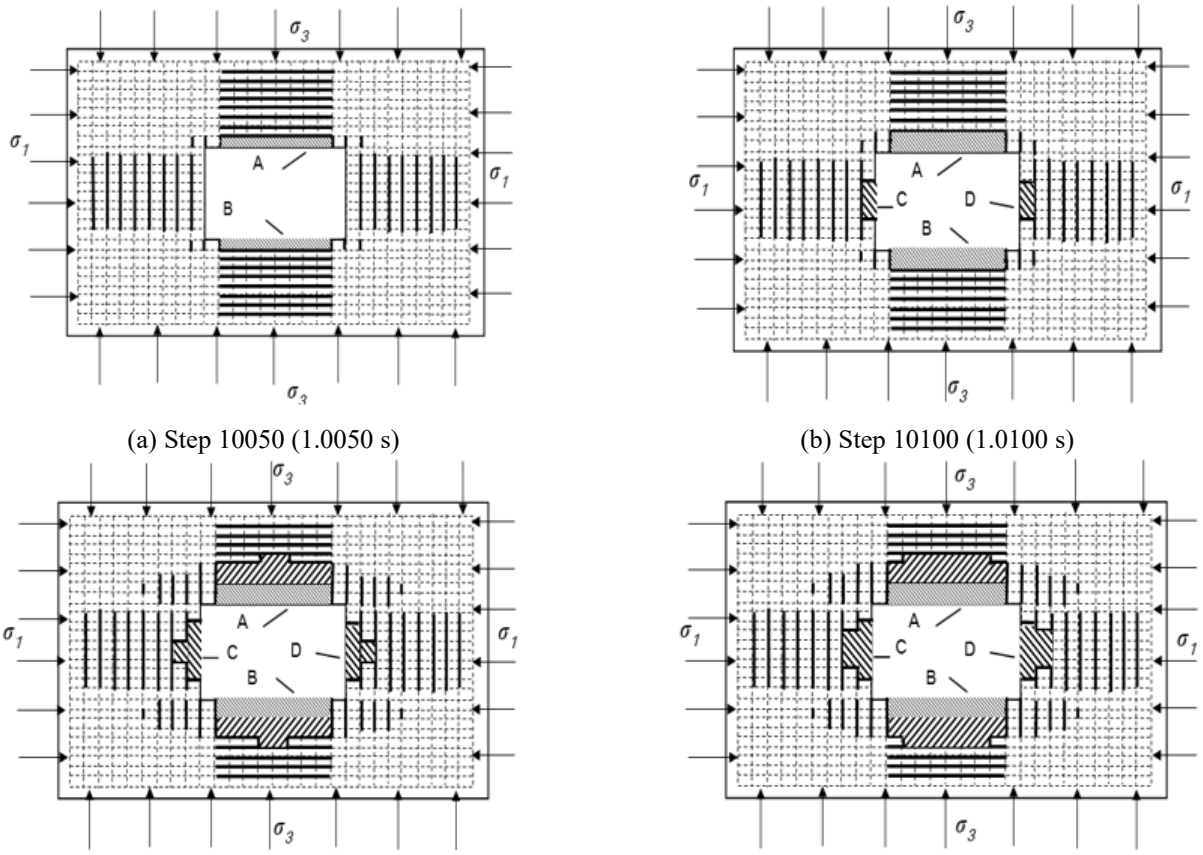

(a) Step 10050 (1.0050 s) (b) Step 10100 (1.0100 s)

(c) Step 10600 (1.0600 s) (d) Step 11500 (1.1500 s)

Fig. 8 Crack propagation pattern after different steps: (a) Step 10050 (1.0050 s), (b) Step 10100 (1.0100 s), (c) Step 10600 (1.0600 s) and (d) Step 11500 (1.1500 s)

deformed sub block in all directions, and the thick solid line shows the cracks generated after the deformed sub block is damaged. The oblique shadow area is a free block that may be separated from the surrounding rock, the fine oblique shadow area (A and B) is flake fragments, and the thick oblique shadow area(C and D) is massive fragments. From this we can see clearly that under the influence of excavation unloading, tensile failure takes place in vertical deformation blocks of the left and right sides and horizontal deformation blocks of the upper and lower sides. A large number of tensile cracks within the surrounding rock and a small number of compressive cracks on the four cross-corners of the tunnel can also be observed (see Fig. 8(a)). In addition, free block zones A and B are formed due to the connection of the vertical cracks and the former tensile cracks. Afterward, tensile failure occurs in the horizontal deformation blocks on the left and right side. As a result, free block zones C and D are formed due to the connection of the tensile cracks and previous vertical cracks (see Fig. 8(b)). It should be noted that at this stage, the tensile strain value decreases from the middle to the sides in free block zones C and D. The depth and area of free block zones A and B still increase due to the continuous extension of the vertical compressive cracks. In the next phase, new free block zones that are farther from the upper and lower sides of the tunnel are formed (see Fig. 8(c)). Note that the strain value decreases from middle to sides in the newly formed free block zones, suggesting rockburst in the form of massive debris will take place in this area. Simultaneously, tensile failure continues to develop to the horizontal deformation blocks on the left and right sides, hence free block zones that are farther from the inner face of the tunnel are formed. Since the effect of rockburst falls off as the distance increases from the inner rock face, the final shape of the free blocks takes on a "V" type distribution. Finally, all deformation blocks fail. As shown in the final crack propagation pattern (see Fig. 8(d)), the generation of free block zones depends mainly on the interpenetration of horizontal and vertical cracks within the surrounding rock. Moreover, it is verified that rockburst zones of different sizes and shapes can form due with different position of the cavern.

3.2.3 Analysis of the velocity-time curve of the block

Figs. 9 and 10 are the respective velocity-time curves of the *x*-direction of block (16, 10) in free block zone C and in the *y*-direction of block (10, 16) in free block zone B. The velocity of block (10, 16) in the *x*-direction is 1.972 m/s when separating from the surrounding rock at 1.01 s. In the same layer, the velocity of block (10, 13) in the *x*-direction is 0.2 m/s when separating from the surrounding rock at 1.03 s. In the second layer, the velocity of block (9, 16) in the *x*-direction is 0.1 m/s. As shown in Fig. 11, in free block zone C, the velocity distribution corresponds to the strain

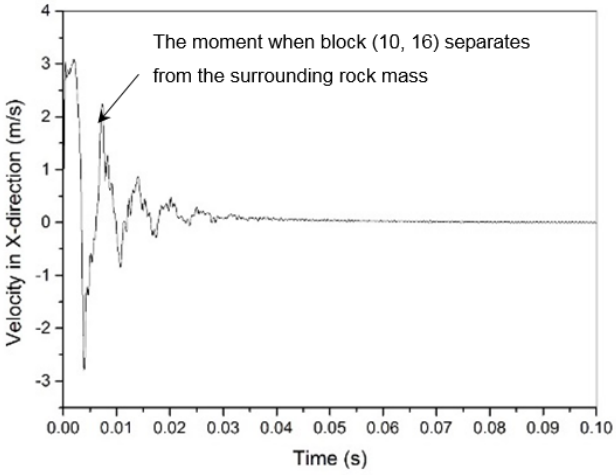

Fig. 9 Time curve of x-direction velocity of block (10, 16)

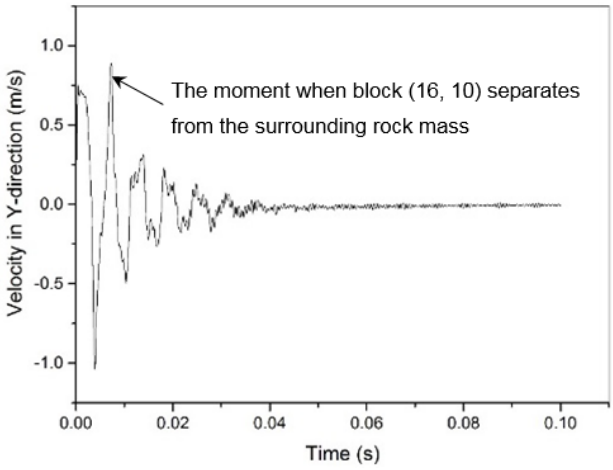

Fig. 10 Time curve of y-direction velocity of block (16, 10)

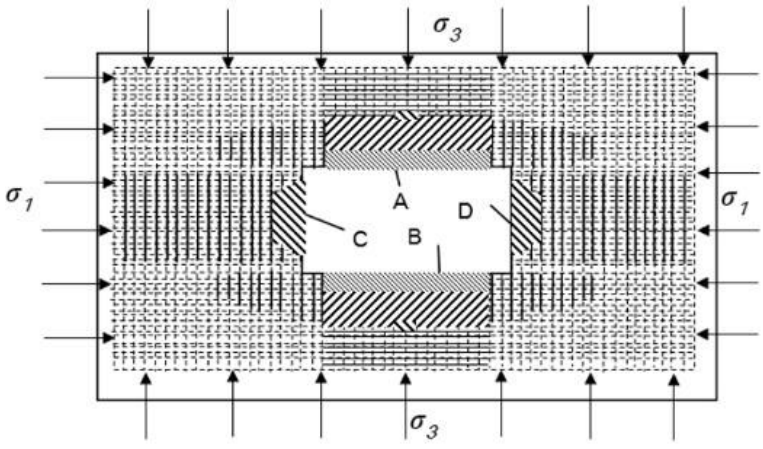

Fig. 11 Crack propagation pattern within the surrounding rock

distribution. From the data above, it is easy to see that for the same layer, the block located in the central part of a rockburst zone has a greater velocity than those in the other parts. Also, a block that is farther from the free face has a relatively smaller velocity. The difference of the initial velocity in horizontal projectile movement forms the scattering appearance of blocks on the ground. For block zone D, the situation is analogous to that of zone C in Fig. 11.

In free block zone B, the velocity of block (16, 10) in

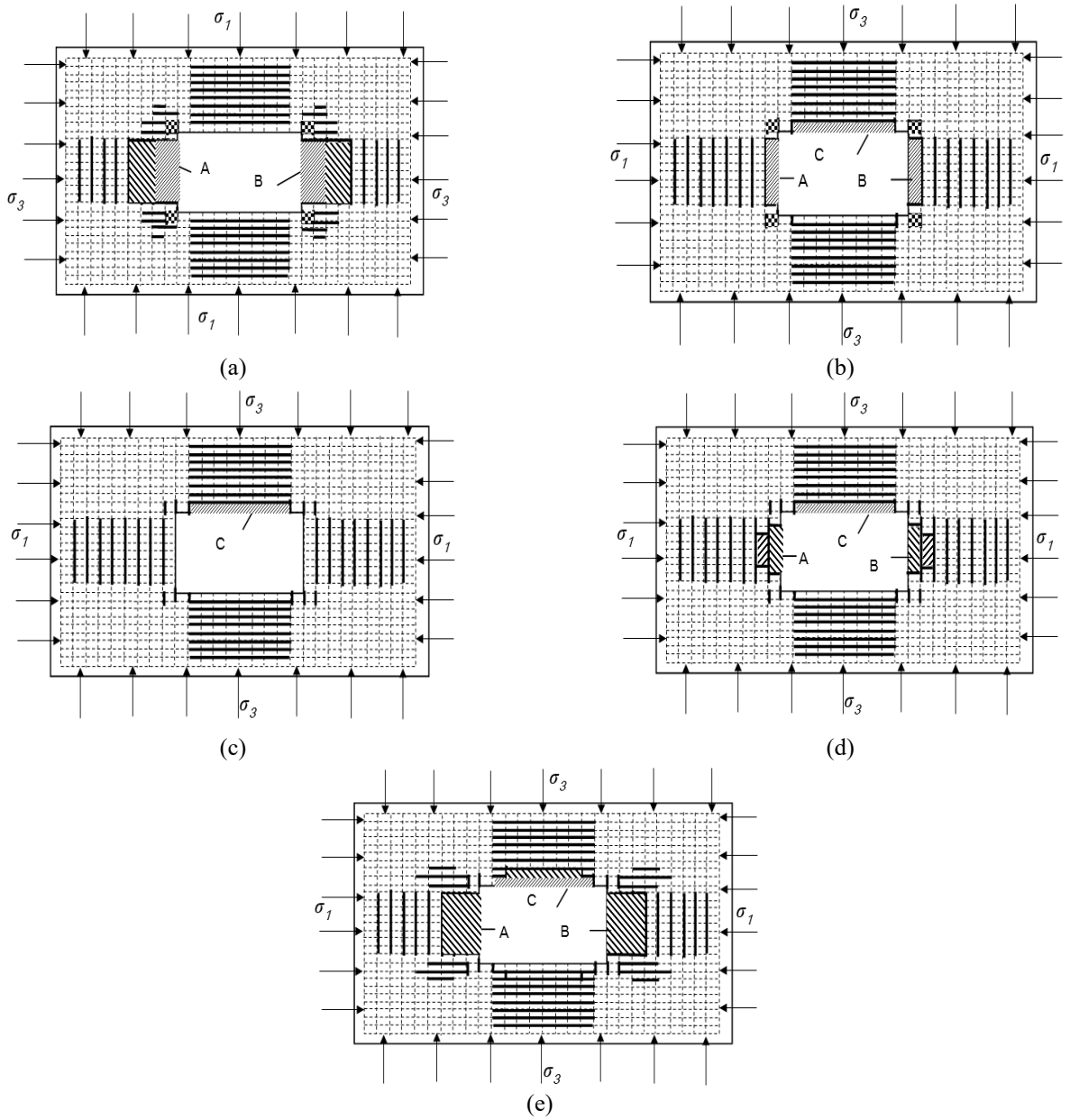

Fig. 12 Prediction results of rockburst under different principal stress ratios; the pictures, in the order presented, correspond to principle ratios (σ_3/σ^1) of 2:3, 1:1, 2:1, 4:1, and 8:1

the *y*-direction is 0.85 m/s. Its kinetic energy can be calculated as follows

$$E_k = \sum_1^n \frac{1}{2} m_i v_i^2 \tag{24}$$

where *m* is the mass of each block, *v* is the velocity vector of each block, and *n* is the number of blocks.

Based on the conservation of energy

$$E_k = \sum \frac{1}{2} mv^2 = Mgh \tag{25}$$

where *M* is the mass of whole blocks in the zone and *h* is the ejection height.

The ejection height for free block zone B is 0.036 m. At the macro level, it shows a slight uplift of the ground. Since it does not conform to the high-speed characteristic of rockburst, free block zone B will not be defined as a rockburst zone. Whereas, for the symmetric al position, rockburst of free block zone A behaves approxi mately in the form of free-fall. From the above, the possible rockburst zones are A, C, and D.

3.3 Influence on rockburst of different principal stress ratios, rock mass parameters

3.3.1 Influence of different principal stress ratios on the intensity of rockburst

Keeping the other parameters invariant, five groups of minor and major principal stresses are set as follows: σ_3 = 120 MPa, σ_1 = 80 MPa; σ_3 = 80 MPa, σ_1 = 80 MPa; σ_3 = 40

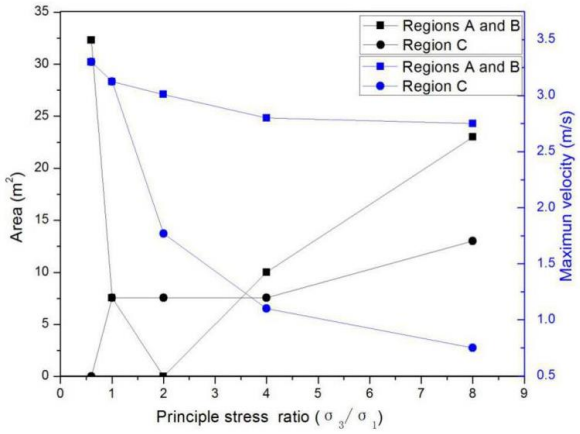

Fig. 13 Variation of rockburst area and maximum velocity under different principal stress ratios

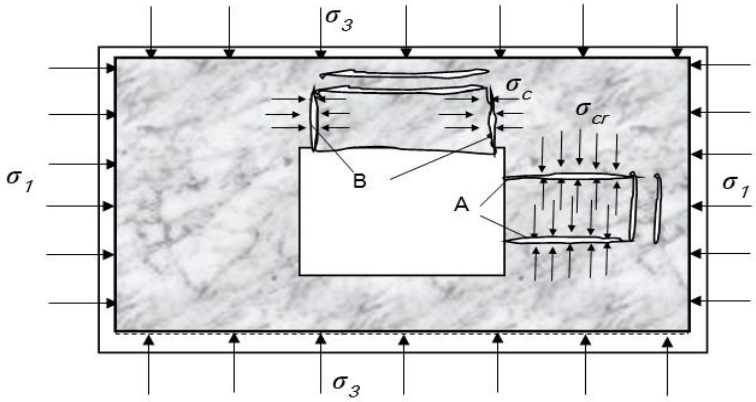

Fig. 14 Analysis of the mechanism underlying the failure of deformation blocks, where Region B and Region A represent the compressive cracks of vertical and horizontal deformation blocks, respectively

MPa, σ_1 = 80 MPa; σ_3 = 20 MPa, σ_1 = 80 MPa; and σ_3 = 10 MPa, σ_1 = 80 MPa. (For the first set, the direction of major principal stress is vertical. For the remaining sets, the direction of major principal stress is horizontal). The values of the principal stress ratio σ_3/σ_1 are 3:2, 1:1, 2:1, 4:1, and 8:1, respectively. The respective directional principal stress ratios σ_x/σ_y are 2:3, 1:1, 2:1, 4:1, and 8:1. The prediction results of rockburst under different principal stress ratios are shown in Fig. 12.

When the principal stress ratio changes from 3:2 (the direction of major principal stress is vertical) to 1:1, as shown in Figs. 12(a) and 12(b), the massive ejection in rockburst zones A and B disappears. The forms of rockburst are mainly flake drops in the upside, left side and right side of the cavern. In the four corners of the rectangular cavern, free block zones are formed (the shadow area in black and white in the figure). Taking the location into consideration, these free blocks cannot get out of the surrounding rock. As the principal stress ratio increases from 1:1 to 8:1 [Figs. 12(b) to 14(e)], for rockburst zone C, the damage form is always flake drops. However, for rockburst zones A and B, the form of rockburst turns from flake drops to massive ejection. In addition, the damage does not appear when the principal stress ratio is 2:1. Meanwhile, a certain number of vertical compressive cracks can be seen in the four corners of the rectangular cavern for all ratios.

Fig. 13 illustrates the changes of rockburst areas and maximum velocity under different principal stress ratios. For zones A and B, the rockburst depth ratios are 0.4, 0.1, 0, 0.2, and 0.3 according to the simulation results, and the corresponding damage areas are 32 m^2, 8 m^2, 0 m^2, 10 m^2, and 24 m^2. Obviously, with the increase of the principal stress ratio, the depth and area of zones A and B first decrease to zero, and then increase. As for zone C, the variations of depth ratio are 0, 0.1, 0.1, 0.1, and 0.2. The corresponding damage areas are 0 m^2, 8 m^2, 8 m^2, 8 m^2, and 14 m^2. The variation tendency of depth and rockburst areas are consistent with the principal stress ratio. In accordance with the depth ratio categorization in the delimitation of the intensity of rockburst proposed by Tan (1991) (see Table 1), when the principal stress ratio is 3:2, extremely intensive rockburst occurs in zones A and B, but there is no rockburst in zone C. When the principal stress ratio increases from 1:1 to 8:1, the rockburst develops from weak to medium level for all rockburst zones. As the principal stress ratio increases, the maximum velocities of zones A and B are 3.35 m/s, 3.13 m/s, 0 m/s, 2.88 m/s, and 2.75 m/s, and for zone C the values are 0 m/s, 3.13 m/s, 1.79 m/s, 1.11 m/s, and 0.77 m/s. Neglecting the zero value, the velocity of all rockburst zones decreases with the decrease of the minor principal stress. According to the velocity categorization in the intensity delimitation of rockburst (Tan 1991), the

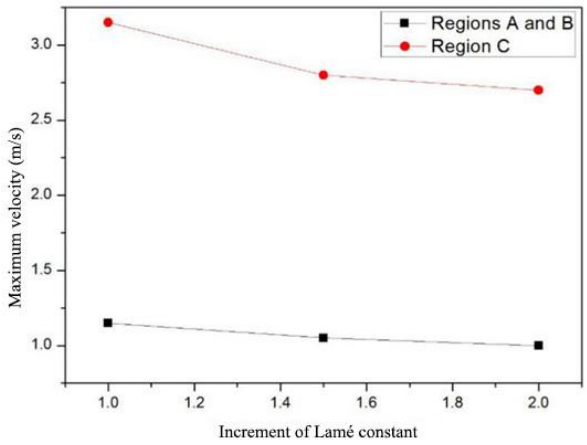

Fig. 15 Variations in the maximum rockburst velocity for different Lamé constants

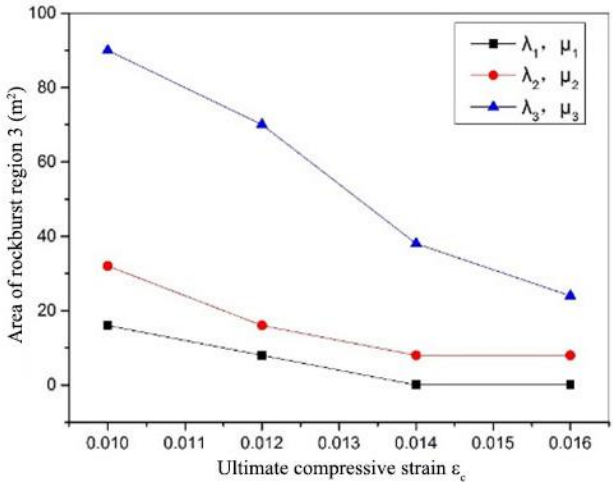

Fig. 16 Area of rockburst region C under different ultimate compressive strains

Table 1 Delimitation of the intensity of rockburst (Tan 1991)

Ruckburst intensity	Weak	Medium	Strong	Extremely strong
Depth ratio	≤0.1	0.1~0.3	0.3~0.5	≥0.5
Width ratio	≤0.25	0.25~0.5	0.5~0.75	≥0.72
Initial velocity	≤2 m/s	2~5 m/s	5~10 m/s	≥10 m/s

rockburst intensity under all the stress ratios in zones A and B belong to the medium level, whereas for zone C, the results vary from medium to weak level. It should be noted that the decreasing tendency of velocity in zone C is much greater than in zones A and B.

The cause of the phenomenon above can be explained by noting that when the major principal stress σ_1 is constant, the compressive strain of the horizontal deformation block (A in Fig. 14) decreases with decreasing minor principal stress σ_3, and the compressive failure of the horizontal deformation block decreases correspondingly. The horizontal deformation block starts to assume a tensile state as the minor principal stress σ_3 decreases to a certain value. Subsequently, tensile cracks initiate gradually when the horizontal deformation block reaches the ultimate tensile strain. In addition, the compressive strain of the vertical deformation block (B in Fig. 14) increases and the compressive cracks grow gradually during the process. This characteristic is similar to the phenomenon in the rock triaxial compression test, in which a decrease of the confining pressure leads to the decline of the axial compressive strength of the rock.

3.3.2 Influence of rock mass parameters on rockburst

The material properties of rock mass are also important factors that influence the intensity of rockburst. Here we choose three groups of Lamé constants as follows: λ_1 = 16 GPa, μ_1 = 8 GPa; λ_2 = 12 GPa, μ_2 = 6 GPa; and λ_3 = 8 Pa, μ_3 = 4 GPa.

Fig. 15 depicts the variation trend of the rockburst maximum velocity with the increase of the Lamé constant. For zones A and B, the rockburst maximum velocities are 3.08 m/s, 2.8 m/s, and 2.65 m/s. For zone C, the values are 1.1 m/s, 1.05 m/s, and 1.02 m/s. The velocities of all rockburst zones decrease gradually. This is because a large amount of the elastic energy disperses among the deformation blocks with the increase of the Lamé constant, and consequently, the strain energy is greatly impaired.

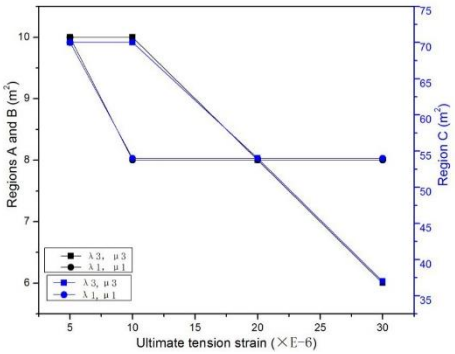

Fig. 17 Area of rockburst regions A, B, and C under different ultimate tension strains

(a) Location of Jinping second hydroelectric power station

(b) Local rockburst events in a certain drainage tunnel

Fig. 18 Introduction of engineering example:(a) Location of the second Jinping hydroelectric power station and (b) local rockburst events in a certain drainage tunnel

Acting as the thresholds in rockburst prediction, the ultimate compressive strain ε_c and tensile strain ε_t play a major role when judging the occurrence of a rockburst. Fig. 16 shows the rockburst area variation in zone C with different ultimate compressive strain values. Fig. 17 shows the area variation in zones A and C under different ultimate tensile strain values. As shown in Figs. 16 and 17, with the increase of ε_c and ε_t, both the rockburst area of zones C and

A decrease as the increment of Lamé constant increases. This is because the number of compressive and tensile cracks that initiate at the unloading moment tend to decrease due to the increase of ultimate compressive and tensile strain threshold.

4. Comparison of results from the analytical solution, numerical simulation, and field-measured data

4.1 Comparison of results of rockburst prediction model for construction drainage tunnel and field measured data

In order to verify the reliability of the proposed analytical calculation mode in this article, this section will compare the results of the construction drainage tunnel rockburst prediction model with the field measured data. Then we compare numerical simulation results using UDEC

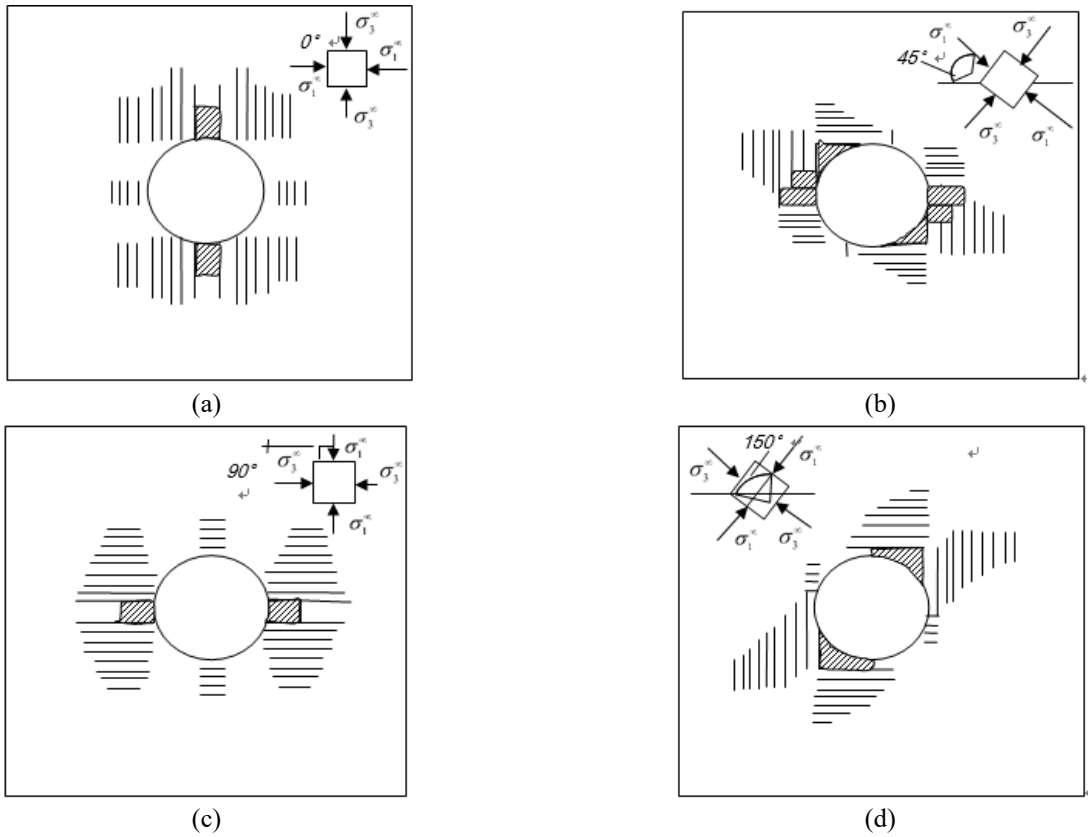

Fig. 19 Rockburst prediction results of circular tunnel

discrete element analytical software and field-measured data of the rockburst for a certain drainage tunnel in the second-cascade hydropower station in Jinping, Sichuan Province, in China (see Fig. 18).

In this section, a circular tunnel with a diameter 7.2 m in the dimensions of 51 m × 51 m is introduced to investigate the influence of a dip of principal stress on rockburst.

The mechanical parameters of the model are set as follows. The block dimensions are L_x=1 m, L_y=1 m, l_x=0.05 m, and l_y=0.05 m. The time step is Δt =0.0001 s. The minimum principal stress is σ_3=32 MPa. The maximum principal stress is σ_1=62 MPa. The block density is ρ=2500 kg/m^3. The Young's modulus and Poisson's ratio of the deformation block are E=20 GPa and v =0.245, respectively. Based on the stress-strain curve of the compression and tensile experiment, the ultimate compressive and tensile strain are set as 0.005 and 0.0001, respectively.

Four sets of dip levels, which are 0°, 45°, 90°, and 150°, are selected, with rockburst prediction results as shown in Fig. 19. When the dip changes from 0° to 90°, the rockburst location gradually moves from the arch to the left and right walls. When the dip changes from 90° to 150°, the rockburst location moves from the left and right walls to the arch again. Fig. 20 describes the variation of the rockburst area and the maximum velocity as the major principal stress dip changes. The rockburst area reaches a maximum value of about 15 m^2 when the principal stress dip is 60° and 120°, and the maximum velocity is 1.88 m/s when the major principal stress dip is 45° and 135°.

According to the results in Figs. 19 and 20, the relationship between the dip of the major principle stress and the rockburst zones can be summarized as follows. Generally, rockburst zones always appear in pairs and symmetrically. When the direction of the major principle stress is vertical or horizontal, the rockburst zones tend to appear in the orthogonal direction to the major principle stress. With the increase or decrease of the dip of the major principal stress, rockburst zones move to a place that is parallel to the direction of major principal stress, but the rockburst area and depth are much smaller than in the former situation, suggesting that horizontal or vertical principal stress conditions are more likely to cause the formation of rockburst.

Furthermore, as shown in Table 2, there is little difference between the calculated location and depth of the rockburst and the field-measured data. The comparisons above indicate that the analytical model proposed in this article can dependably predict the occurrence of rockburst.

4.2 Comparison of rockburst prediction model simulation results of construction drainage tunnel with UDEC rockburst simulation

As shown in Fig. 21, the UDEC prediction model is 60 m x 60 m, and the diameter of the central circular tunnel is 7.2 m. Detailed rock mass parameters are presented in Table 3. Horizontal and vertical virtual joints at 0.5-m intervals are set in a 25 m x 25 m area around the rock mass. Then the geostress is exerted at each boundary and the tunneling process is started after the initial forces come to a balanced condition.

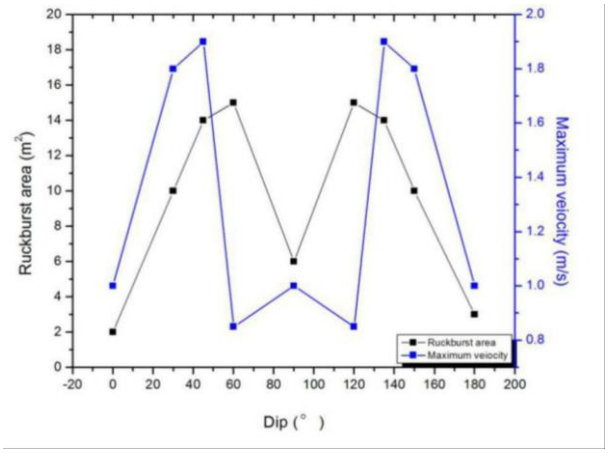

Fig. 20 Variation of rockburst area and maximum velocity under different major principal stress dips

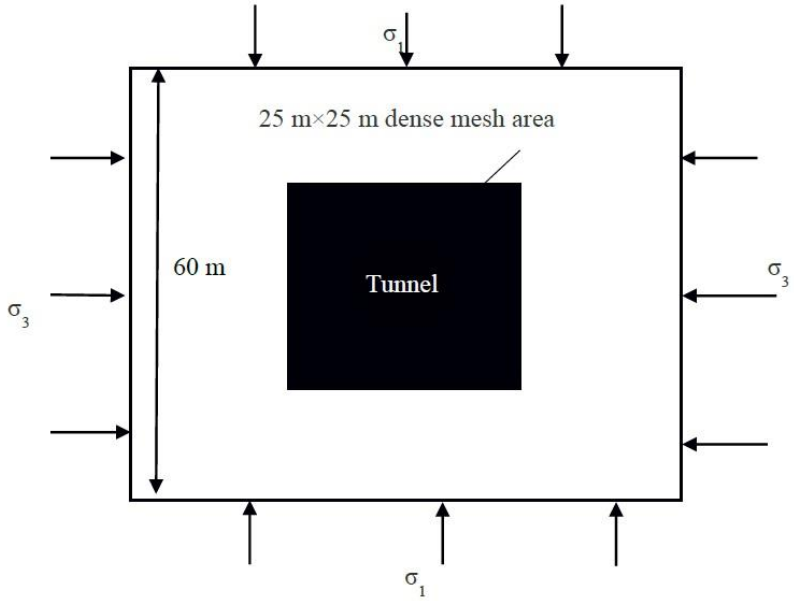

Fig. 21 Rockburst prediction model in UDEC

Table2 Comparison table of field data and prediction model at SK-14 section (Liu *et al*. 2011)

Stake number (m)	Surrounding rock mass level	Rockburst location		Rockburst depth(m)	
		Measured	This article	Measured	This article
SK14+415-14+390	III	Right wall	Left and right walls, vault	1.8	3(Left and right walls) 2(vault)
SK14+415-14+390	III	Left wall, vault	Left and right walls, vault	2.1	3(Left and right walls) 2(vault)
SK14+230-14+227	II	Right spandrel	Right spandrel	1.5	1.5(Right spandrel)
SK14+252-14+250	III	Right spandrel	Left and right walls, right spandrel	1.0	1.5(Right spandrel) 1(Left and right walls)

According to measured data of the studied area, the most likely principle stress dip angles of 120°, 135°, and 150° are selected in the comparison analysis. The rockburst prediction results of the UDEC simulation model and the analytical method in this article are provided in Fig. 22. To be specific, when the principle dip angle is 120°, rockburst mainly occurs in the left and right walls. At 135°, rockburst areas appear on the left wall and right spandrel initially,

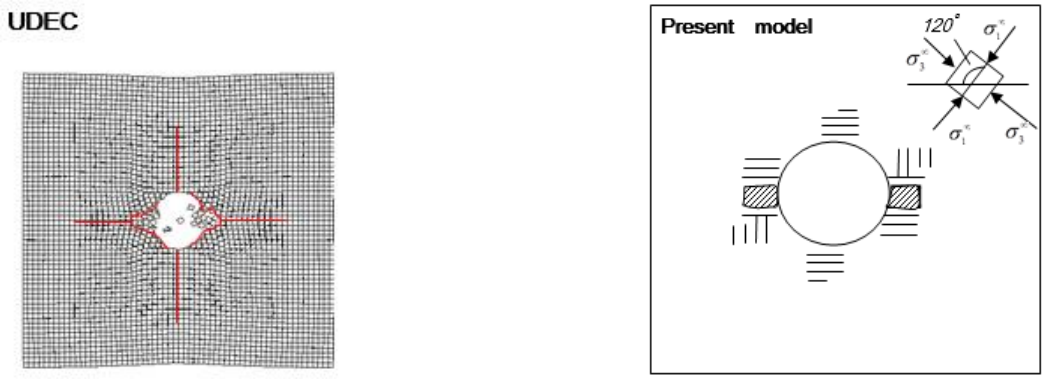

(a) Principle stress dip angle of 135°

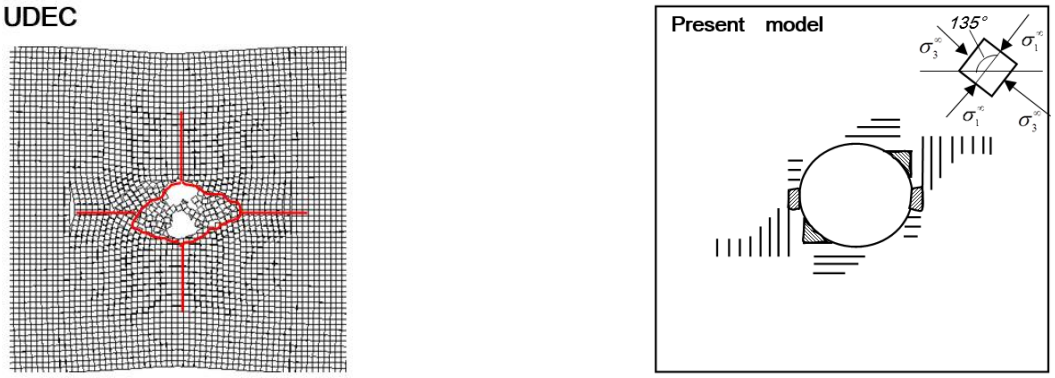

(b) Principle stress dip angle of 120°

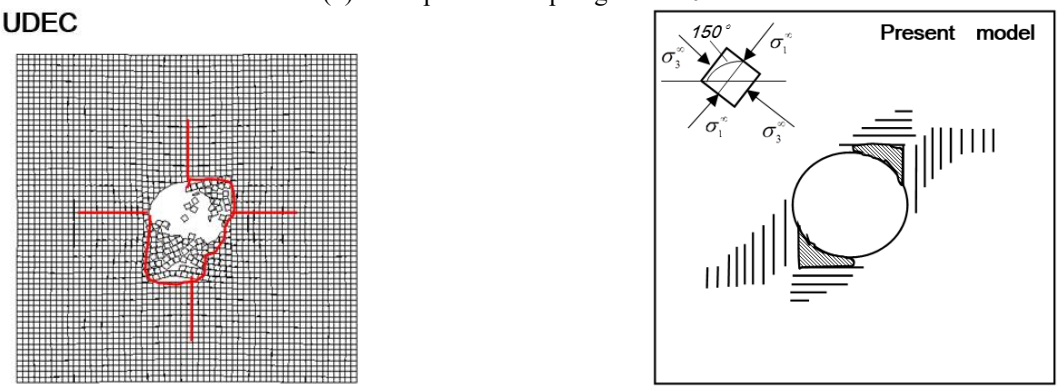

(c) Principle stress dip angle of 150°

Fig. 22 Rockburst prediction under different dip angles by UDEC and present model: (a) Principle stress dip angle of 135°, (b) principle stress dip angle of 120°, (c) principle stress dip angle of 150°

Table 3 Physical and mechanical parameters of rock mass in UDEC model

	Normal stiffness (GPa)	Shear stiffness (GPa)	Frictional angle	Cohesive force (MPa)	Tensile Strength (MPa)
Block	14.255	12.44	/	/	/
Discontinuous surface original value	10	10	42	2	1
Discontinuous surface residue value	5	5	12	0.1	0

then extend to the right wall and right haunch. When the dip angle is 150°, rockburst takes place on the right haunch and right spandrel, and then extends to the vault. The simulation results show good agreement with the analytical solution of the present model.

Fig. 23 shows the comparison of the maximum rockburst depth and rockburst area obtained by this model and UDEC model. As shown in Fig. 23, the difference between the maximum pit depth obtained by the rockburst prediction model in this paper and the results obtained by

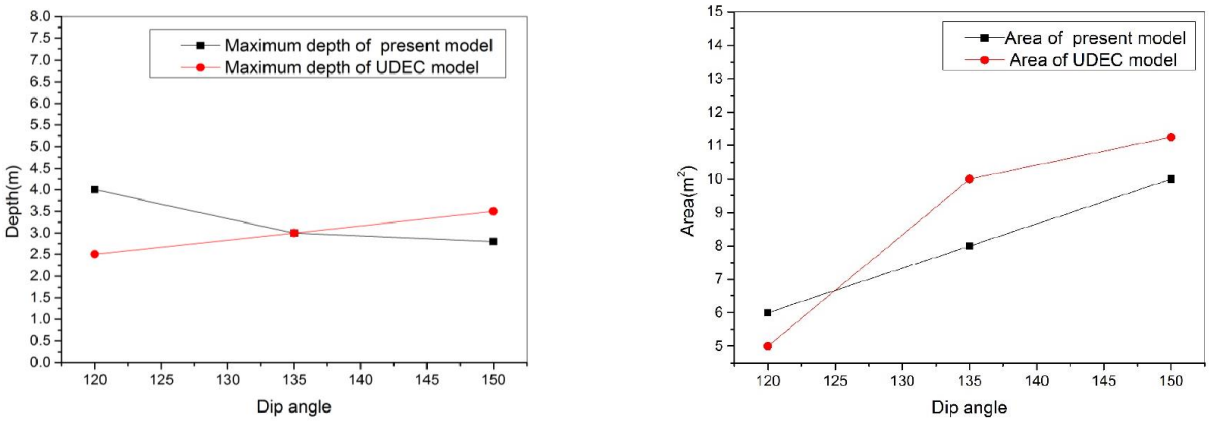

Fig. 23 The rockburst prediction of maximum depth and area under different dip angle by present model and UDEC model

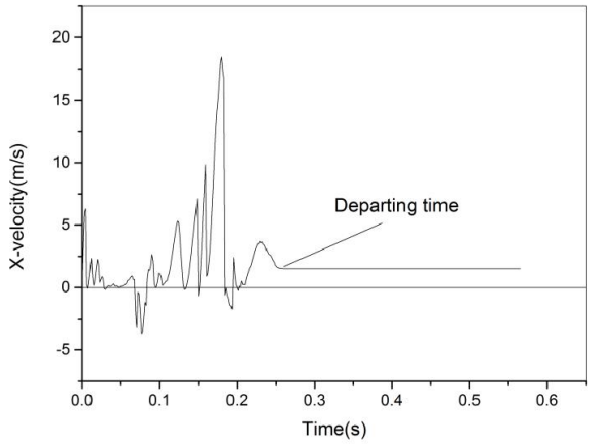

Fig. 24 The time curve of velocity of block (34,31) in x direction

UDEC simulation is 25%, which occurs at 120°. The maximum difference between the results of the two models is 20%, which occurs at 135° Fig. 24 is the horizontal velocity time history of the block (34,31) at the lower position of the right spandrel at 150°. The horizontal velocity of the block when it is separated from the parent rock is 1.51 m/s. In Fig. 20, the velocity of the model at 150° is 1.357 m/s, and the difference is within 10%. This verifies the feasibility of the model in this paper to predict the range, depth and velocity of rockburst.

5. Conclusions

Based on the two-dimensional discontinuous block model, a prediction model has been established to reproduce the initiation process of anomalously low friction-type rockbursts. The investigation of this paper reveals that rockburst is a characteristic of the rock mass and is mainly affected by the brittle property of the rock material and by geostress. Based on the numerical simulation results, the following conclusions can be drawn.

- As the principal stress ratio increases, the mechanism of the rockburst zone which is parallel to the direction of the principal stress transforms from compressive damage to tensile damage, and the depth ratio and rockburst area decrease first, and then increase. However, the mechanism of the rockburst zone that is vertical to the direction of the principal stress is always compressive damage, and both the depth ratio and rockburst area increase invariably. For all the rockburst zones, the maximum velocity decreases during the process. Furthermore, the influence of geostress is more obvious for rockburst depth and area in the compressive zone than in the tensile zone. In addition, the increase of the Lamé constant is unfavorable for the occurrence of rockburst. Also, with the increase of the compressive strain threshold, areas of all rockburst zones decrease, but with the increase of the tensile strain threshold, only the rockburst area that is vertical to the principle stress decreases. Finally, rockburst is more likely to take place when the major principal stress is in the vertical or horizontal direction. The conclusion in this paper shows good consistency with Kaiser's opinion (Kaiser 1996), which considers that a mass of cracks may initiate and propagate when the stress exceeds the strength of the rock mass, and as a result the volume of rock mass expends sharply, then rockburst is formed due to the sudden release of the elastic energy inside the rock mass. The prediction result indicates that the location, rockburst depth, damage area, and maximum velocity of the block can be obtained by using the anomalously low friction-type rockburst prediction model.

- The model presented in this paper can be used as a tool to predict rockburst. Nevertheless, some deficiencies exist. For example, this model considers only rectangular and uniform blocks, which will result in many limitations in its practical application. Also, to obtain realistic results, the influence of elasto-plastic behavior of a rock mass remains to be extensively studied. Moreover, we would like to extend the present model to consider detailed geological factors.

Acknowledgements

The research described in this paper was financially supported by the National Natural Science Foundation of China (NO. 41202195, 41672290, 52008111) and Natural Science Foundation of Fujian province NO. 2016J01189.

References

Aleksandrova, N.I. and Sher, E.N. (2004), "Modeling of Wave Propagation in Block Media", *J. Min. Sci.*, **40**(6), 579-587.

Chen, B.R., Feng, X.T., Li, Q.P., Luo, R.Z. and Li, S. (2015), "Rock burst intensity classification based on the radiated energy with damage intensity at Jinping II hydropower station, China", *Rock Mech. Rock Eng.*, **48**(1), 289-303. https://doi:10.1007/s00603-013-0524-2.

Di, Y. and Wang, E. (2021), "Rock burst precursor electromagnetic radiation signal recognition method and early warning application based on recurrent neural networks", *Rock Mech. Rock Eng.*, **54**(3), 1449-1461. https://doi:10.1007/S00603-020-02314-W.

Dorigo, M. and Birattari, M. (2010), "Ant colony optimization. Encyclopedia of Machine Learning", Springer US: 36-39.

He, B.G., Zelig, R., Hatzor, Y.H. and Feng, X.T. (2016), "Rockburst generation in discontinuous rock masses", *Rock Mech. Rock Eng.*, **10**(49), 4103-4124. https://doi:doi:10.1007/s00603-015-0906-8.

He, M., Ren, F. and Liu, D. (2018), "Rockburst mechanism research and its control", *Int. J. Min. Sci. Technol.*, **28**(5), 829-837. https://doi.org/10.1016/j.ijmst.2018.09.002.

Hoek, E. and Brown, E.T. (1980), "Underground Excavation in Rock", Institute of Mining and Metallurgy, London.

Huang, M., Xu, C.S., Zhan, J.W. and Wang, J.B. (2017), "Comparative study on dynamic properties of argillaceous siltstone and its grouting-reinforced body", *Geomech. Eng.*, **13**(2), 333-352. https://doi:10.12989/gae.2017.13.2.333.

Ji, B., Xie, F., Wang, X., He, S. and Song, D. (2020), "Investigate contribution of multi-microseismic data to rockburst risk prediction using support vector machine with genetic algorithm", *IEEE Access*, **8**, 58817-58828. https://doi: 10.1109/ACCESS.2020.2982366.

Kaiser, P.K., Tannant, D.D. and McCreath, D.R. (1996), "Canadian rockburst support handbook", ON: Geomechanics Research Centre, Laurentian University, Sudbury.

Kazarinov, N.A., Petrov, Y.V. and Cherkasov, A.V. (2021), "Instability effects of the dynamic crack propagation process", *Eng. Fract. Mech.*, **242**, 107438. https://doi:10.1016/J.ENGFRACMECH.2020.107438.

Keneti, A. and Sainsbury, B.A. (2018), "Review of published rockburst events and their contributing factors", *Eng. Geol.*, **246**, 361-373. https://doi.org/10.1016/j.enggeo.2018.10.005.

Kidybinski, A. (1981), "Bursting liability indices of coal", *Int. J. Rock Mech. Sci.*, **18**(4), 295-304. https://doi.org/10.1016/0148-9062(81)91194-3.

Kurlenya, M.V., Oparin, V.N. and Vostrikov, V.I. (1998), "Geomechanical conditions for quasi-resonances in geomaterials and block material", *J. Min. Sci.*, **34**(5), 379-386.

Lei, X., Kusunose, K. and Rao, M. (2000), "Quasi–static fault growth and cracking inhomogeneous brittle rock under triaxial compression using acoustic emission monitoring", *J. Geophys. Res.*, **105**(3), 6127-6139. https://doi.org/10.1029/1999JB900385.

Li, C.C., Mikula, P., Simser, B., Hebblewhite, B., Joughin, W., Feng, X. and Xu, N. (2019), "Discussions on rockburst and dynamic ground support in deep mines", *J. Rock Mech. Geotech. Eng.*, **11**(5), 1110-1118. https://doi.org/10.1016/j.jrmge.2019.06.001.

Liu, L.P., Wang, X.G. and Jia, Z.X. (2011), "Analysis of mechanism and characteristic of rockburst in drainage-hole of Jinping II hydropower station", *J. Central South Univ.* (Science and Technology), **42**(10), 3150-3155. https:// https://doi.org/10.CNKI:SUN:ZNGD.0.2011-10-044.

Ma, T.H., Tang, C.A., Tang, S.B., Kuang, L., Yu, Q., Kong, D.Q. and Zhu, X. (2018), "Rockburst mechanism and prediction based on microseismic monitoring", *Int. J. Rock Mech. Min. Sci.*, **110**, 177-188. https://doi.org/10.1016/j.ijrmms.2018.07.016.

Manouchehrian, A. and Cai, M. (2017), "Analysis of rockburst in tunnels subjected to static and dynamic loads", *J. Rock Mech. Geotech. Eng.*, **9**(6), 1031-1040. https://doi:10.1016/j.jrmge.2017.07.001.

Mazaira, A. and Konicek, P. (2015), "Intense rockburst impacts in deep underground construction and their prevention", *Can. Geotech. J.*, **52**(10), 1426-1439. https://doi:10.1139/cgj-2014-0359.

Pu, Y., Apel, D.B., and Xu, H. (2019), "Rockburst prediction in kimberlite with unsupervised learning method and support vector classifier", *Tunn. Undergr. Sp. Tech.*, **90**, 12-18. https://doi.org/10.1016/j.tust.2019.04.019.

Pu, Y., Apel, D.B., Liu, V., and Mitri, H. (2019), "Machine learning methods for rockburst prediction-state-of-the-art review", *Int. J. Min. Sci Technol.*, **29**(4), 565-570. https://doi.org/10.1016/j.ijmst.2019.06.009.

Russense, B.F. (1974), "Analysis of rock spalling for tunnels in steep valley sides", Yüksek Lisans Tezi.

Sadovsky, M.A. (1979), "Natural lumpiness of rocks", Dokl Akad Nauk SSSR, **247**(4): 21-29.

Sadovsky, M.A. (1979), "Natural lumpiness of rocks", Dokl Akad Nauk SSSR, **247**(4): 21-29.

Saraikin, V.A., Stepanenko, M.V. and Tsareva, O.V. (1988), "Elastic waves in a medium with block structure", *J. Min. Sci.*, **24**(1), 11-17.

Sepehri, M., Apel, D.B., Adeeb, S., Leveille, P. and Hall, R.A. (2020), "Evaluation of mining-induced energy and rockburst prediction at a diamond mine in Canada using a full 3D elastoplastic finite element model", *Eng. Geol.*, **266**, 105457. https://doi:10.1016/j.enggeo.2019.105457.

Shen, B., Stephansson, O., Rinne, M., Amemiya, K., Yamashi, R., Toguri, S. and Asano, H. (2011), "FRACOD modeling of rock fracturing and permeability change in excavation-damaged zones", *Int. J. Geomech.*, **11**(4): 302-313. https://doi:10.1061/(ASCE)GM.1943-5622.0000034..

Shi, J.W. and Chen, Z.L. (2014), "Based on Numerical Simulation Study of Rockburst in Roadway Induced by Fault", Advanced Materials Research. Trans Tech Publications, 962:370-374. https://doi: 10.4028/www.scientific.net/AMR.962-965. 370.

Shi, X., Wang, M., Wang, Z., Wang, Y., Lu, S. and Tian, W. (2021), "A brittleness index evaluation method for weak-brittle rock by acoustic emission technique", *J. Natural Gas Sci. Eng.*, **95**, 104160. https://doi.org/10.1016/j.jngse.2021.104160.

Slepyan, L.I. (2012), "Models and Phenomena in Fracture Mechanics", Springer-Verlag, Berlin–Heidelberg.

Stacey, T.R. (2016), "Addressing the consequences of dynamic rock failure in underground excavations", *Rock Mech Rock Eng*., **10**(49), 4091-4101. https://doi:10.1007/s00603-016-0922-3.

Tan, Y., Sun, G.Z. and Guo, Z.H. (1991), "A composite index Krb criterion for the ejection characteristics of the burst rock", *Sci. Geol. Sin*., **2**, 193-200. https://doi:CNKI:SUN:DZKX.0.1991-02-009.

Turchaninov, I.A. (1981), "Condition of extra hard rock into weak under the influence of tectonic stress of massifs", Int. Symposium Weak Rock, Tokyo :555-559.

Ulusay R. (2016), "Rock mechanics and rock engineering: From the past to the future", CRC Press. https://doi.org/10.1201/9781315388502.

Wang, C., Cao, C., Liu, Y., Li, C., Li, G. and Lu, H. (2021), "Experimental investigation on synergetic prediction of rockburst using the dominant-frequency entropy of acoustic emission", *Nat. Hazards*, 1-18. https://doi:10.1007/S11069-021-04822-6.

Wang, C., Wu, A., Lu, H., Bao, T. and Liu, X. (2015), "Predicting rockburst tendency based on fuzzy matter–element model", *Int. J. Rock Mech. Min. Sci*., **75**, 224-232. https://doi.org/10.1016/j.ijrmms.2015.02.004.

Wang, C.L., Chuai, X. S., Shi, F., Gao, A. and Bao T. (2018), "Experimental investigation of predicting rockburst using Bayesian model", *Geomech. Eng*., **15**(6), 1153-1160. https://doi:10.12989/gae.2018.15.6.1153.

Wang, X., Li, S., Xu, Z., Xue, Y., Hu, J., Li, Z. and Zhang, B. (2019), "An interval fuzzy comprehensive assessment method for rock burst in underground caverns and its engineering application", *Bull. Eng. Geol. Environ*., **78**(7), 5161-5176. https://doi:10.1007/s10064-018-01453-3.

Wu, H., Fang, Q. and Wang, H.L. (2008), "Mechanism of anomalously low friction phenomenon in deep block rock mass", *Chin J. Geotech. Eng.,* **30**, 769-775.

Xue, Y., Bai, C., Kong, F., Qiu, D., Li, L., Su, M. and Zhao, Y. (2020). "A two-step comprehensive evaluation model for rockburst prediction based on multiple empirical criteria", *Eng. Geol.*, **268**, 105515. https://doi.org/10.1016/j.enggeo.2020.105515.

Yang, Y., Zhang, D., Li, S., Yang, L. and Jin, L. (2019). "In-situ stress test and rockburst analysis in Micang Mountain tunnel. Energy Sources", *Part A: Recovery, Utilization, and Environ. Effects*, 1-10. https://doi.org/10.1080/15567036.2019.1649748.

Yu D., Peng, J., Cui, C. and Sun, Z. (2010), "Complete stress-strain process and mechanical of lamellar rock under compression condition", *J. Basic Sci. Eng*., **18**(5), 792-800. https://doi:CNKI:SUN:YJGX.0.2010-05-009.

Zhou, J., Li, X. and Mitri, H.S. (2016), "Classification of rockburst in underground projects: comparison of ten supervised learning methods", *J. Comput. Civil Eng.,* **30**(5), 04016003. https://doi:10.1061/(ASCE)CP.1943-5487.0000553.

Zou, J.F. and Su, Y. (2016), "Theoretical solutions of a circular tunnel with the influence of the out-of-plane stress based on the generalized hoek–brown failure criterion", *Int. J. Geomech,*, **16**(3), 06015006. https://doi:10.1061/(ASCE)GM.1943-5622.0000547.

Zuo, Y.J., Xu, T., Zhang, Y.B., Zhang, Y.P., Li, S.C., Zhao, G.F. and Chen, C.C. (2012), "Numerical study of zonal disintegration within a rock mass around a deep excavated tunnel", *Int. J. Geomech*., **12**(4), 471-483. https://doi:10.1061/(ASCE)GM.1943-5622.0000155.